Check for updates

Microflower-like $Co_9S_8@MoS_2$ heterostructure as an efficient bifunctional catalyst for overall water splitting†

Chaohai Pang, [iD] ‡*[ab] Xionghui Ma, [iD] ‡[ab] Yuwei Wu,[ab] Shuhuai Li, [iD] *[ab] Zhi Xu,[ab] Mingyue Wang[ab] and Xiaojing Zhu*[c]

The development of a distinguished and high-performance catalyst for H_2 and O_2 generation is a rational strategy for producing hydrogen fuel *via* electrochemical water splitting. Herein, a flower-like $Co_9S_8@MoS_2$ heterostructure with effective bifunctional activity was achieved using a one-pot approach *via* the hydrothermal treatment of metal-coordinated species followed by pyrolysis under an N_2 atmosphere. The heterostructures exhibited a 3D interconnected network with a large electrochemical active surface area and a junctional complex with hydrogen evolution reaction (HER) catalytic activity of MoS_2 and oxygen evolution reaction (OER) catalytic activity of Co_9S_8, exhibiting low overpotentials of 295 and 103 mV for OER and HER at 10 mA cm^{-2} current density, respectively. Additionally, the catalyst-assembled electrolyser provided favourable catalytic activity and strong durability for overall water splitting in 1 M KOH electrolyte. The results of the study highlight the importance of structural engineering for the design and preparation of cost-effective and efficient bifunctional electrocatalysts.

Introduction

Owing to increasing energy demands and the unreasonable use of fossil fuels, there is an urgent need for clean and sustainable energy.[1] The development of sustainable, inexpensive, eco-friendly, and highly efficient energy resources is one of the most effective approaches for resolving environmental and energy problems. Electrocatalytic water splitting to H_2 and O_2 is an attractive and highly potential technology for renewable energy production because water resources are abundant and no carbon is involved.[2,3] The catalytic performance of precious catalysts, such as platinum[4] and RuO_2/IrO_2,[5–7] remains unmatched for electrocatalytic water splitting. Nevertheless, prohibitive cost, scarcity, and poor durability of these precious catalysts restrain their large-scale practical applications.[8–10] Consequently, it is tremendously desirable to prepare high-

efficiency and low-cost bifunctional catalysts for overall water splitting.[11,12]

Recently, various investigations have shown that MoS_2 is a promising candidate for the HER.[13–16] However, MoS_2 also has drawbacks such as covering of active sites, poor conductivity, and low OER performance.[17–19] In contrast, transition metal sulphides and oxides of Co such as Co_3S_4,[20,21] Co_9S_8,[22–24] Co_4O_4,[25] and $LaCoO_3$[26,27] exhibit higher conductivity and efficient electrocatalytic performance for the OER, but their HER performance is unsatisfactory. Some studies have reported that the electronic structure of MoS_2 can be modulated and optimised by doping with transition metals (*e.g.* Ni and Co) to achieve enhanced catalytic activity.[28,29] Consequently, the integration of OER-active Co_9S_8 and HER-active MoS_2 into the same material is a judicious strategy for fabricating suitable bifunctional electrocatalysts for water electrolysis.[30]

Several studies are currently focusing on the fabrication of bifunctional electrocatalysts comprising MoS_2 and Co_9S_8 nanocomposites to achieve efficient overall water splitting.[23,31–35] Cao *et al.*[17] prepared a uniform $Co_9S_8@MoS_2$ heterostructure using a simple process that combined solvothermal treatment with pyrolysis. In an alkaline solution, the proposed heterostructure showed a current density of 10 mA cm^{-2} for the HER and OER under overpotentials of 143 and 340 mV, respectively. Meanwhile, for overall water splitting, only a voltage of 1.67 V was demanded at 10 mA cm^{-2} in alkaline electrolyser. Du *et al.*[36] designed and prepared a multicomponent $Co_9S_8@MoS_2$ nanohybrid derived from cobalt-doped polyoxometalate using a one-pot calcination technique. This

[a] Analysis and Test Center, Chinese Academy of Tropical Agricultural Sciences, Hainan Provincial Key Laboratory of Quality and Safety for Tropical Fruits and Vegetables, Key Laboratory of Quality and Safety Control for Subtropical Fruit and Vegetable, Ministry of Agriculture and Rural Affairs Haikou, 571101, China. E-mail: 18389859589@163.com; happylishuhuai@163.com

[b] Key Laboratory of Tropical Fruits and Vegetables Quality and Safety for State Market Regulation, Haikou, 570311, China

[c] Research Center of Advanced Chemical Equipment, Chemistry and Chemical Engineering Guangdong Laboratory, Shantou 515041, China. E-mail: xiaoj_zhu@163.com

† Electronic supplementary information (ESI) available. See https://doi.org/10.1039/d2ra04086g

‡ C. P and X. M contributed equally to this work.

nanohybrid exhibited a smallish overpotential (230 mV) for the OER but a relatively high overpotential (239 mV) for the HER at 10 mA cm^{-2}. Despite these advances, it is necessary to develop a novel and simple route to obtain cost-efficient bifunctional electrocatalysts with unique structures for the sake of enrichment of material preparation database, remarkable performance, and robust stability.

In this study, a bifunctional hybrid electrocatalyst comprising Co_9S_8 and MoS_2 with the structural merits of a flower-like morphology was synthesised using a facile hydrothermal treatment with metal salts and the strongly coordinating ligand ethylenediamine and formaldehyde, followed by annealing. A three-dimensionally interconnected network structure with the Co_9S_8 microflower tightly attached to the MoS_2 nanoflakes was materialised. The obtained $Co_9S_8@MoS_2$ heterostructure was further explored as bifunctional electrocatalysts for HER and OER. Compared with the sole component of Co_9S_8 and MoS_2, the prepared $Co_9S_8@MoS_2$ microflowers displayed low overpotentials of 295 and 103 mV to achieve a current density of 10 mA cm^{-2} in alkaline electrolyte for the HER and OER, respectively, as well as a low overpotential (1.64 V) for overall water splitting at a current density of 10 mA cm^{-2} when employed as a two-electrode assembly device. The results in this work highlight the importance of structural engineering for the design and preparation of low-cost, efficient, and bifunctional electrocatalysts.

Results and discussion

The two-step synthesis method for $Co_9S_8@MoS_2$ is illustrated in Fig. 1a. First, a flower-like composite precursor was formed by hydrothermal treatment of the metal salts in the presence of the strongly coordinating ligands thiourea, ethylenediamine, and formaldehyde.[37] Subsequently, the sample was pyrolyzed in a tube furnace under a nitrogen ambiance at 500 °C to obtain the $Co_9S_8@MoS_2$ heterostructure. The SEM images in Fig. 1b reveal that $Co_9S_8@MoS_2$ comprised flower-like structures, which is uniform spherical with a regular size of ~2.0 μm. In contrast, MoS_2 comprised aggregated nanosheets with no clear macroporous structures (Fig. 1c). Co_9S_8 exhibits a flower-like morphology similar to that of $Co_9S_8@MoS_2$, but unexpected spherical particles are also present on the surface of the Co_9S_8 microflowers, indicative that the addition of Mo salt allows the surface coverage and keep the structural integrity (Fig. 1d). These morphology differences demonstrate the success assemble of MoS_2 and Co_9S_8 in the one flower-like component. Notably, the intact flower-like morphology of the $Co_9S_8@MoS_2$ composite implies that the formation of spherical particles was hindered by the surface coverage of MoS_2 nanosheets during carbonisation. Furthermore, the porous texture of $Co_9S_8@MoS_2$ can provide abundant channels for the release of electrolyte and gaseous products.

The $Co_9S_8@MoS_2$ has a porous flower-like morphology comprising interconnected flakes with a thickness of approximately 20 nm (Fig. 2a and b). Fig. 2c shows that the $Co_9S_8@MoS_2$ particles comprised a dense inner Co_9S_8 layer and outer MoS_2 nanosheets. Lattice fringes with spacings of 0.30 and 0.62 nm are clearly visible in the High-Resolution TEM (HRTEM) images, which correspond to the (311) plane of Co_9S_8 and the (002) plane of MoS_2. In addition, the lattice fringes between Co_9S_8 and MoS_2 are clearly observed (Fig. 2e and f). Elemental mapping (Fig. 2g) confirms that Mo, S, and Co are evenly distributed in the $Co_9S_8@MoS_2$ heterostructure.

The three-dimensional (3D) flower-like $Co_9S_8@MoS_2$ heterostructural spheres are assembled by the interconnections of heterostructural 2D nanosheets, which not only prevent the
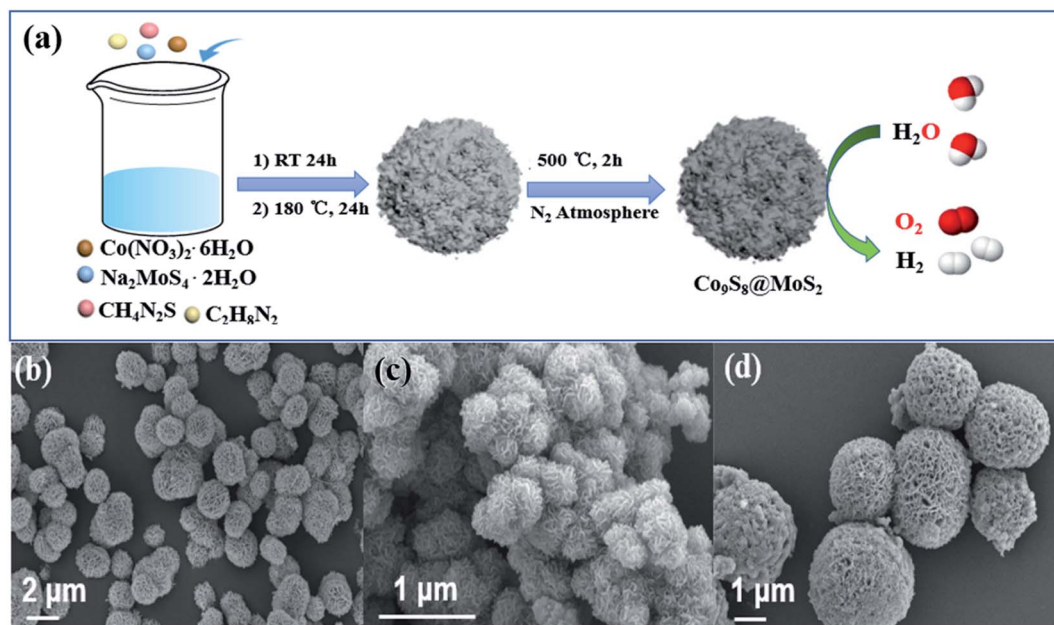

Fig. 1 (a) Schematic illustration of the fabrication of a typical sample $Co_9S_8@MoS_2$ as a bifunctional electrocatalyst for water splitting. SEM images for $Co_9S_8@MoS_2$ (b), MoS_2 (c) and Co_9S_8 (d).

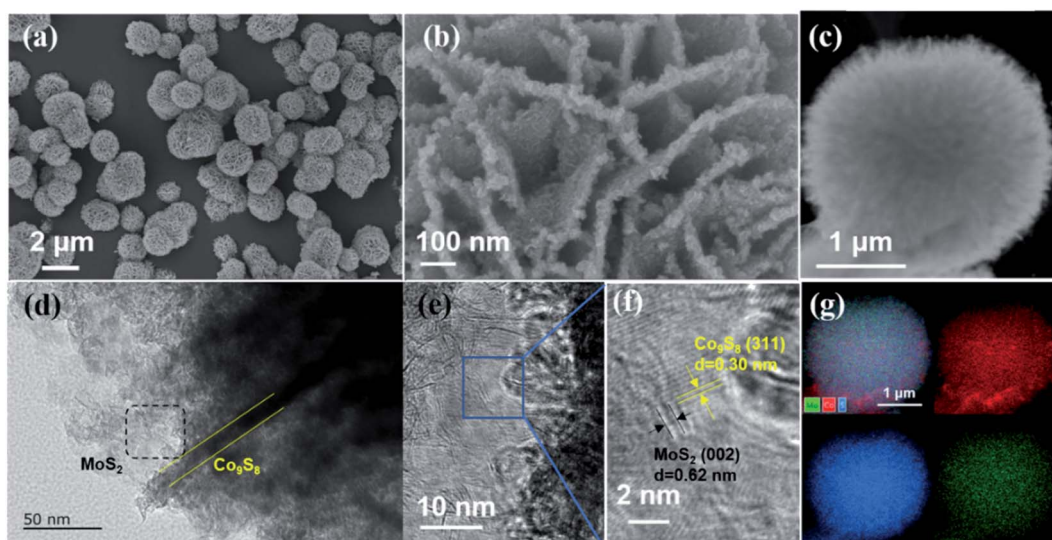**Fig. 2** The characteristics of Co_9S_8@MoS_2: (a and b) SEM images with different magnification; (c) HADDF–STEM image; (d) TEM image; (e and f) HR–TEM images and (g) overlap of elemental maps of Mo, Co, and S.

restack/aggregation of nanosheets but also provide hierarchical three-dimensional porous structures, allowing the well-exposed interfaces and favourable diffusion channels and manifesting excellent electrocatalytic performance for overall water.

To obtain in-depth understanding of the elemental states and phase structures of the Co_9S_8@MoS_2 composite, XPS and powder XRD investigations were performed. The XRD pattern of Co_9S_8@MoS_2 in Fig. 3a exhibits characteristic diffraction peaks at 14.2°, 32.8°, 33.8°, 39.6°, 49.5°, and 58.9°, which can be attributed to the (002), (100), (101), (102), (110), and (008) planes, respectively, of MoS_2 (PDF#37-1492). In addition, the peaks at 29.8°, 47.5°, and 52.1° were well-matched with the (311), (511), and (440) planes, respectively, of Co_9S_8 (PDF#19-0364).

The XPS survey spectrum (Fig. S1†) of as-prepared Co_9S_8@MoS_2 sample reveals the presence of Mo, Co, and S, which is in agreement with the XRD and EDS mapping results. In Fig. 3b, it is obvious that the high-resolution spectrum of Co 2p is deconvoluted into two spin–orbit doublets. The first doublet at 778.7 eV (Co $2p_{3/2}$) and 793.7 eV (Co $2p_{1/2}$) is assigned to Co^{3+}, whereas the second doublet at 781.1 eV (Co $2p_{3/2}$) and 797.3 eV (Co $2p_{1/2}$) is assigned to Co^{2+}. Further, the signals displayed at 802.4 and 786.3 eV are typical satellite peaks.[38,39] In Fig. 3c, the peak at 228.8 eV is attributed to Mo $3d_{5/2}$, and the peak at 232.5 eV is ascribed Mo $3d_{3/2}$. The two weak peaks signal at 225.8 and 226.5 eV are assigned to the S 2s shoulder peak, revealing that the S species bonded to Mo and Co ions have two chemical phases.[40] In the S 2p spectrum (Fig. 3d), the significant peaks at 161.2 and 162.7 eV are ascribed to S $2p_{3/2}$ and S $2p_{1/2}$ of Co_9S_8@MoS_2, whereas the peaks at 161.5 and 163.8 eV are attributed to S $2p_{3/2}$ and S $2p_{1/2}$ of MoS_2.[41] Notably, as shown in Fig. 3e and f, the binding energy of the Co 2p3/2 from Co_9S_8@MoS_2 exhibits positive shifts of ∼0.6 eV relative to that pure Co_9S_8 while the Mo $3d_{5/2}$ and Mo $3d_{3/2}$ peaks in Co_9S_8@MoS_2 display ∼0.6 eV down-shift compared to the pure MoS_2, further

confirming the existence of Co_9S_8@MoS_2 heterostructure with strong electronic interactions between Co_9S_8 and MoS_2. This change in binding energies preliminarily proves that the electrons are transferred from Co to Mo, which results in more negative charged Mo species generation and enhanced catalytic activity. Additionally, the Co_9S_8@MoS_2 microflowers show a high specific surface area up to 157.0 m² g⁻¹ and hierarchical porous structure with meso- and microporosity (Fig. S2†).

In 1 M KOH, the electrocatalytic performance of Co_9S_8@MoS_2 for the OER was assessed. The individual Co_9S_8 and MoS_2 materials were also examined for comparison. In addition, as a well-known OER catalyst, IrO_2 was used as a benchmark. Fig. 4a illustrates representative polarisation curves for the various catalysts. The OER evaluation results of the catalyst decrease in the following order Co_9S_8@MoS_2-iR > Co_9S_8@MoS_2 > Co_9S_8 > IrO_2 > MoS_2. The potential required by Co_9S_8@MoS_2 (1.525 V) to achieve at 10 mA cm⁻² is found to be lower than those required by IrO_2 (1.558 V), Co_9S_8 (1.558 V), and MoS_2 (1.692 V). Based on the Tafel slopes derived from the linear sweep voltammetry curves (Fig. 4b), Co_9S_8@MoS_2 exhibits the fastest kinetics for oxygen production. The Tafel slope for Co_9S_8@MoS_2 (175 mV dec⁻¹) is lower than those of Co_9S_8 (177 mV dec⁻¹), MoS_2 (265 mV dec⁻¹), and even IrO_2 (194 mV dec⁻¹). In the Nyquist plots (Fig. 4c), a semicircle appears at high frequencies corresponding to the charge-transfer resistance. The diameter of this semicircle is smaller for Co_9S_8@MoS_2 than for Co_9S_8, MoS_2, and IrO_2, indicating a lower charge-transfer resistance of the composite material.[42] It is worth mentioning that, the *in situ* generated CoOOH of cobalt-based catalyst, which certainly include Co_9S_8@MoS_2 and Co_9S_8,[17,43] is generally claimed to be the actual active center for OER electrocatalysis.[44–47] In our study, the exposable density of active sites and charge-transfer resistance of the transformed CoOOH-containing catalyst are mainly determining the OER electrocatalytic activity, not involving the dominated high intrinsic
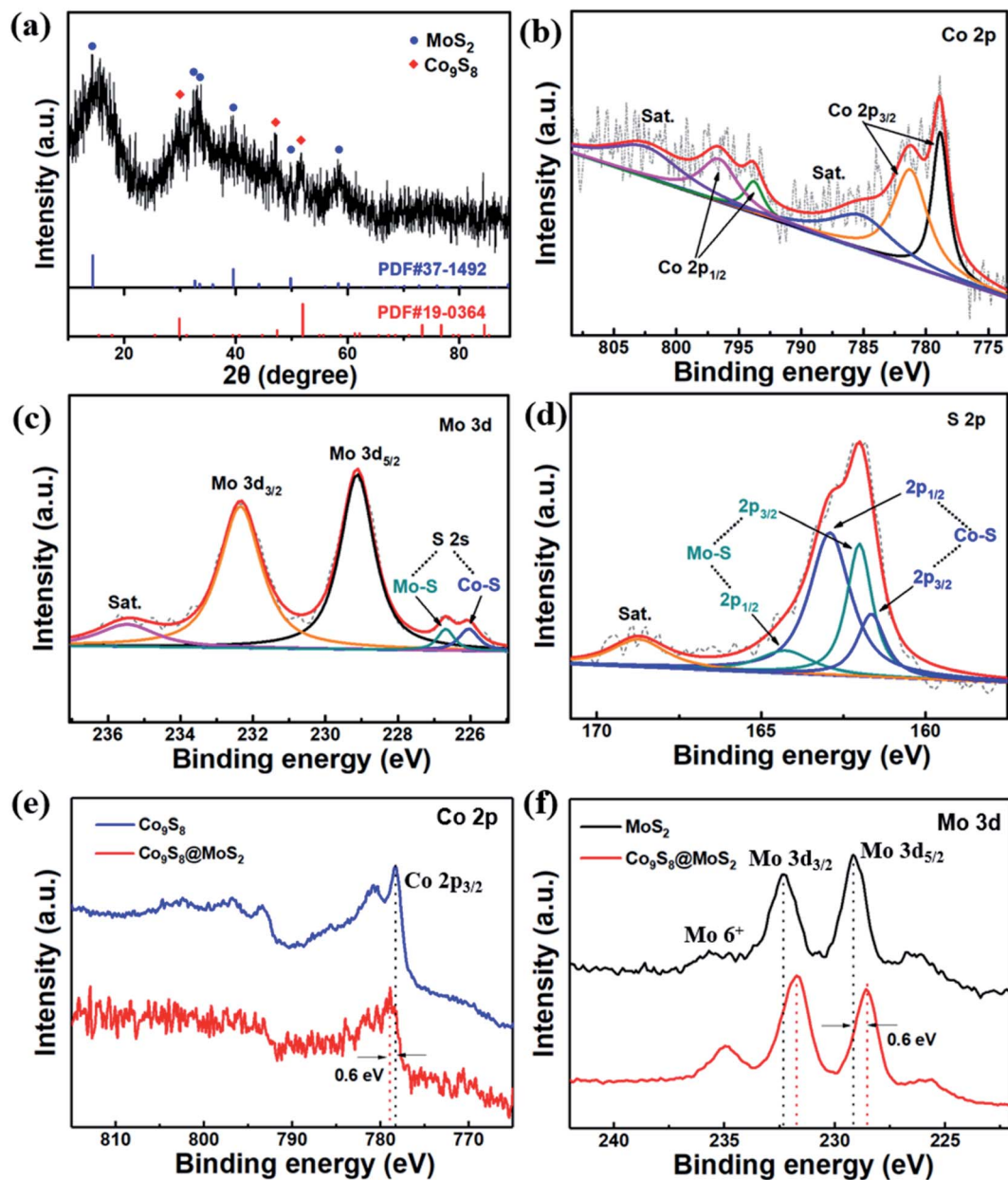
Fig. 3 XRD pattern of the prepared $Co_9S_8@MoS_2$ (a). The blue and red vertical lines indicate reference patterns of MoS_2 (PDF card no. 37-1492) and Co_9S_8 (PDF card no. 19-0364), respectively. High-resolution XPS spectra of (b) Co 2p, (c) Mo 3d, and (d) S 2p of $Co_9S_8@MoS_2$. The contrast of (e) Co 2p spectra in $Co_9S_8@MoS_2$ and Co_9S_8, and (f) Mo 3d spectra in $Co_9S_8@MoS_2$ and MoS_2.

activity tuned by defect engineering and heteroatomic doping.[44,48] Consequently, due to the nanostructural virtues of 3D porous framework and heterojunctions, the CoOOH-containing catalyst transformed from $Co_9S_8@MoS_2$ shows the low charge-transfer resistance and high exposed active site, resulting in slightly enhanced OER activity. These results also founded by the previous reported literatures.[3,17,40]

Durability and stability are also key parameters for estimating the electrocatalytic capability of $Co_9S_8@MoS_2$. The chronoamperometric responses (i–t) of catalysts were recorded at an applied potential of 1.558 V ($vs.$ RHE). As demonstrated in Fig. 4d, the decrease in the current density of $Co_9S_8@MoS_2$ over

15 h is insignificant than that of IrO_2, showing the robust durability of $Co_9S_8@MoS_2$. To further understand the stability of the $Co_9S_8@MoS_2$, the SEM technique was performed after the OER test. As shown in the Fig. S3†, after the above long-time OER test, $Co_9S_8@MoS_2$ can largely retained its original morphology, although a slight aggregation and surface collapse is observed, indicative of its excellent structural stability. The excellent stability of $Co_9S_8@MoS_2$ can be ascribed to its unique heterostructures: (i) the interfacial interaction between Co_9S_8 and MoS_2 enhances the density of electron transfer at the joint boundaries; (ii) a unique core–shell nanostructure is constructed by the highly active Co_9S_8 core, along with a more
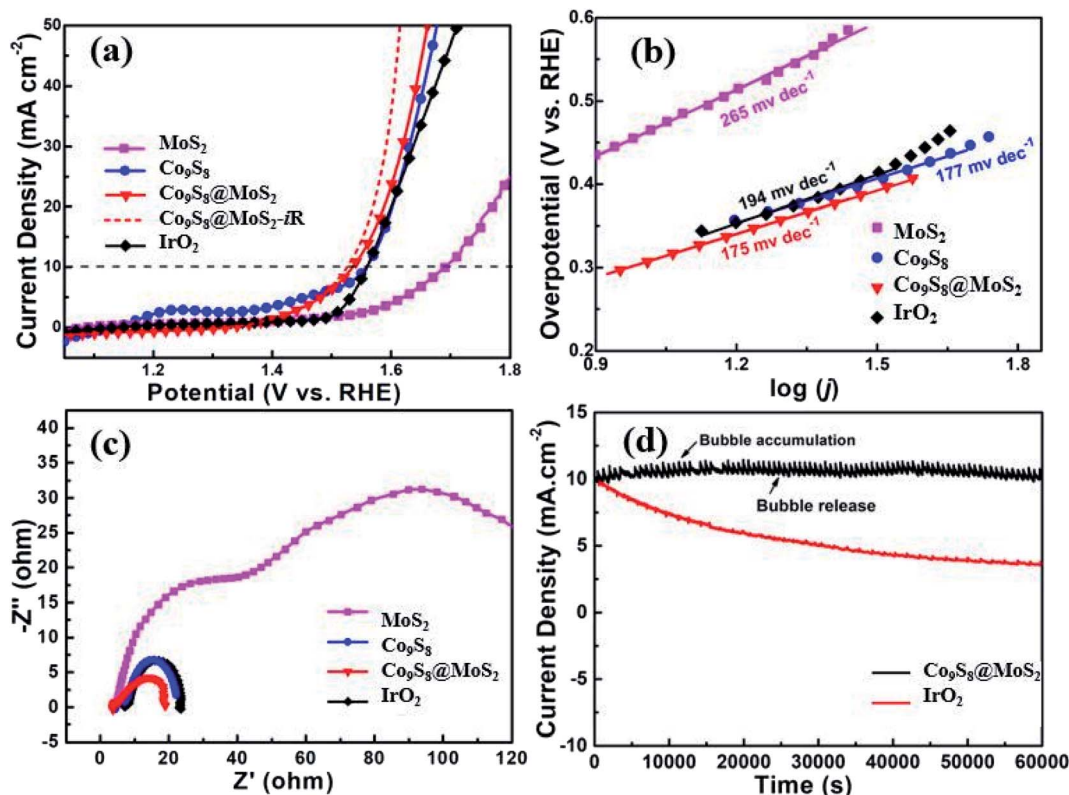
Fig. 4 (a) LSV curves and (b) the corresponding Tafel plots of $Co_9S_8@MoS_2$, $Co_9S_8@MoS_2$ with iR compensation ($Co_9S_8@MoS_2$-iR), MoS_2, Co_9S_8, and IrO_2 electrodes for OER in a 1 M KOH electrolyte. (c) Electrochemical impedance spectra of different electrodes at +1.56 V for OER with an AC amplitude of 5 mV within the frequency range of 100 kHz to 0.01 Hz. (d) Chronoamperometric responses (i−t) collected on the $Co_9S_8@MoS_2$ electrode and IrO_2 at the same current density of 10 mA cm^{-2} in 1 M KOH aqueous solution.

stable MoS_2 shell; (iii) the 3D flower-like porous framework enables the easy release of bubbles formed on the surface of the electrode during operation, thus preventing the electrocatalyst from being removed from the electrode.

Similarly, the HER performance of Co_9S_8, MoS_2, and $Co_9S_8@MoS_2$ was assessed in 1 M KOH; a 20% Pt/C was also tested for comparison. Fig. 5a exhibits the polarisation curves of Co_9S_8, MoS_2, $Co_9S_8@MoS_2$, iR-corrected $Co_9S_8@MoS_2$, and Pt/C obtained at a scan rate of 10 mV s^{-1} in 1 M KOH. Notably, the Pt/C exhibits superior HER activity, which merely need an overpotential of 54 mV at 10 mA cm^{-2}. While the HER activity of $Co_9S_8@MoS_2$ is weaker than that of Pt/C, it exhibits a lower overpotential (η_{10} = 103 mV) than MoS_2 (η_{10} = 323 mV) and Co_9S_8 (η_{10} = 228 mV). The Tafel slopes (Fig. 5b) are estimated to be 336, 129, 124, and 67 mV dec^{-1} for MoS_2, Co_9S_8, $Co_9S_8@MoS_2$, and Pt/C. As shown by the Nyquist plots in Fig. 5c, the charge-transfer resistance of $Co_9S_8@MoS_2$ is evidently lower than those of MoS_2 and Co_9S_8, which is favourable for the HER. This remarkable enhanced HER activity for $Co_9S_8@MoS_2$ is mainly due to its porous three-dimensional flower-like heterostructure spheres and the interfacial areas triggering electron transfer that can significantly increase the exposal of active sites and activates HER electrocatalysis.[3,23,31] Moreover, the chronoamperometric curve in Fig. 5d exhibits that $Co_9S_8@MoS_2$ is stable for more than 16 h and its microflower-like morphology

can unambiguously observed in the SEM images taken after continuously catalyzing HER (Fig. S4†). In addition, in an acidic medium, the $Co_9S_8@MoS_2$ electrode also exhibits remarkable HER activity, requiring a low potential of 114 mV at 10 mA cm^{-2} (Fig. S5†).

To determine the origin of the remarkable HER property of $Co_9S_8@MoS_2$ in an alkaline solution, the electrochemically active surface areas (ECSAs) of the catalysts are considered. The electrochemical double-layer capacitance (C_{dl}) is positively correlated with the electrochemical surface area,[14,49] therefore, the ECSA of each catalyst is estimated from the C_{dl} value, as calculated using the cyclic voltammetry curves obtained at a series of scan rates (20 to 100 mV s^{-1}) in the non-faradaic reaction range. As observed in Fig. S6†, the C_{dl} value of Co_9S_8 (27.4 mF cm^{-2}) and MoS_2 (1.8 mF cm^{-2}) is lower than that of $Co_9S_8@MoS_2$ (40.0 mF cm^{-2}) in 1 M KOH. Thus, it is observed that $Co_9S_8@MoS_2$ exhibits outstanding electrocatalytic performance.

To further explicitly explain the effect of MoS_2 concentration toward electrocatalytic HER and OER performance, two counterparts $Co_9S_8@MoS_2$ with varying MoS_2 concentration were prepared by feeding the different amount of Molybdenum salt and denoted as $Co_9S_8@MoS_2$-low and $Co_9S_8@MoS_2$-high. The electrochemical activities of $Co_9S_8@MoS_2$ with different MoS_2 concentration were investigated in alkaline media for OER and

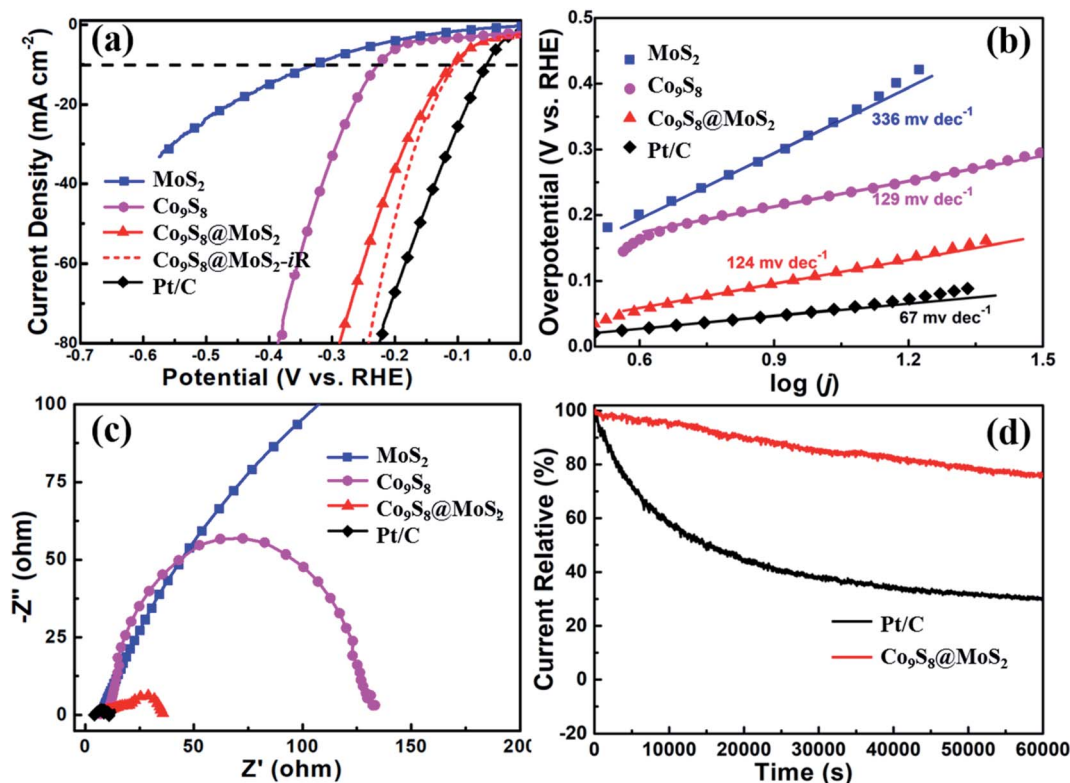**Fig. 5** (a) LSV curves and (b) the corresponding Tafel plots of $Co_9S_8@MoS_2$, $Co_9S_8@MoS_2$ with iR compensation ($Co_9S_8@MoS_2$-iR), MoS_2, Co_9S_8, and Pt/C electrodes for HER in a 1 M KOH electrolyte. (c) Electrochemical impedance spectra of different electrodes at −0.28 V for HER with an AC amplitude of 5 mV within the frequency range of 100 kHz to 0.01 Hz. (d) Chronoamperometric plots for comparing the operation stability of $Co_9S_8@MoS_2$ and Pt/C electrodes at the applied potential of −103 mV and −54 mV ($vs.$ RHE), respectively.

HER. As shown in Fig. S7†, $Co_9S_8@MoS_2$-low exhibits the worst performances for both OER and HER may owing to its thin MoS_2 nanosheets or less active sites on the interfaces of Co_9S_8 and MoS_2. Although $Co_9S_8@MoS_2$-high demonstrates a favorable improved the activities for both OER and HER compared to those exhibited by $Co_9S_8@MoS_2$-low, it still displays the lower catalytic activities as compared with that of $Co_9S_8@MoS_2$. This can be due to excessive MoS_2 is coated on the surface of Co_9S_8, which obstruct the activity of the inner Co_9S_8 layer.[38] Thus,

$Co_9S_8@MoS_2$ heterostructure with an optimal concentration of MoS_2 were studied systematically in present work.

The above findings indicate that $Co_9S_8@MoS_2$ is a satisfactory electrocatalyst for both the OER and the HER. In a two-electrode setup, $Co_9S_8@MoS_2$ was used as both the anode and the cathode, and its catalytic performance for water splitting was assessed in 1 M KOH. In Fig. 6a, the $Co_9S_8@MoS_2$ electrode exhibits excellent performance, attaining water splitting at 10 mA cm^{-2} under a low voltage of 1.64 V. Moreover, the long-term
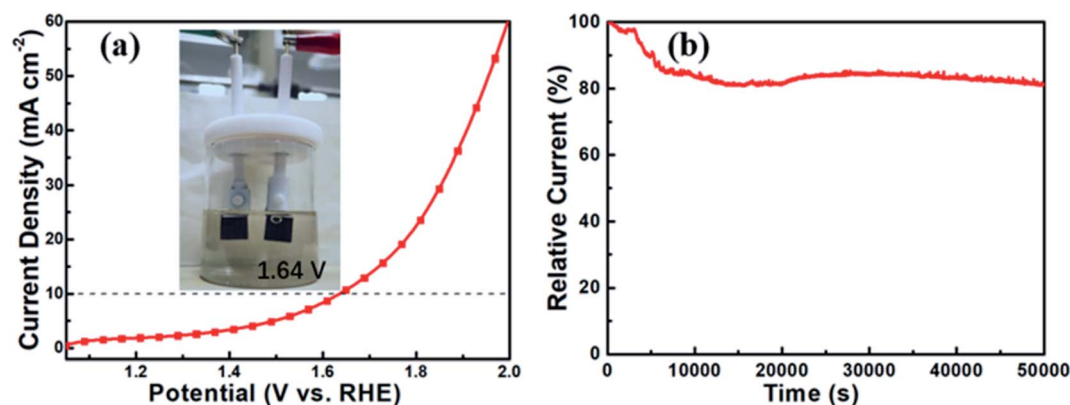

Fig. 6 (a) LSV curves of $Co_9S_8@MoS_2$ as a bifunctional catalyst in 1 M KOH for overall water splitting; inset to panel (a) is the illustration of the two-electrode setup for overall splitting. (b) The stability of the $Co_9S_8@MoS_2$ on carbon cloth at a voltage of 1.64 V.

stability over 12 h was measured using chronoamperometry (Fig. 6b). The current density degraded only slightly, indicating the noteworthy stability of the $Co_9S_8@MoS_2$ electrode for the water splitting reaction.

Thus, the flower-like $Co_9S_8@MoS_2$ heterostructure obtained in this study possesses unique structural merits such as a hierarchical 3D porous framework and a 2D sheet-like heterojunction structure, which facilitate short diffusion channels and well-exposed active sites, showing a high electrochemical active area and low electrochemical impedance. These features afford remarkable bifunctional electrocatalytic performance and stability for the HER and OER, which compares favourably to contemporary nonprecious metal or leading cobalt- and molybdenum-based electrocatalysts (Table S1†).

Conclusions

A $Co_9S_8@MoS_2$ bifunctional catalyst was designed and synthesised using a two-step process that combined a hydrothermal reaction and thermal annealing. During this process, surface coverage by MoS_2 nanosheets hindered the formation of spherical Co_9S_8 particles, and the obtained porous structure was advantageous for electrolyte infiltration and the transportation of intermediates. The flower-like $Co_9S_8@MoS_2$ heterostructure incorporated MoS_2 as a stable HER catalyst of MoS_2 and Co_9S_8 as a notable OER catalyst. Thus, $Co_9S_8@MoS_2$ acted as a bifunctional catalyst with a low charge-transfer resistance and a high ECSA. $Co_9S_8@MoS_2$ exhibited low overpotentials of 103 and 114 mV for the HER at 10 mA cm^{-2} under alkaline and acidic conditions, respectively. Moreover, the OER performance of $Co_9S_8@MoS_2$ was satisfactory, and an overpotential of only 295 mV was required at 10 mA cm^{-2}. Moreover, for water splitting, a low voltage of 1.64 V was achieved by employing the microflower-like $Co_9S_8@MoS_2$ electrocatalyst as a two-electrode setup. The findings of this study provide insights for fabricating high-performance bifunctional electrocatalysts with advantageous structures for overall water splitting.

Author contributions

Chaohai Pang: conceived and designed the experiments. Chaohai Pang and Xiaojing Zhu: Performed the experiments. Chaohai Pang and Xionghui Ma: Analyzed the data. Chaohai Pang: writing – original draft. Xiaojing Zhu, Yuwei Wu and Shuhuai Li: writing – review & editing. Zhi Xu and Mingyue Wang: supervision, funding acquisition and project administration. All authors have discussed and given approval to the final version of the manuscript.

Conflicts of interest

There are no conflicts to declare.

Acknowledgements

References

1 S. Chu and A. Majumdar, *Nature*, 2012, **488**, 294–303.

2 X. Zou and Y. Zhang, *Chem. Soc. Rev.*, 2015, **44**, 5148–5180.

3 Y. Li, C. Wang, M. Cui, J. Xiong, L. Mi and S. Chen, *Appl. Surf. Sci.*, 2021, **543**, 148804.

4 J. Greeley, T. F. Jaramillo, J. Bonde, I. Chorkendorff and J. K. Nørskov, *Nat. Mater.*, 2006, **5**, 909–913.

5 S. Cherevko, S. Geiger, O. Kasian, N. Kulyk, J. P. Grote, A. Savan, B. R. Shrestha, S. Merzlikin, B. Breitbath, A. Ludwig and K. J. J. Mayrhofer, *Catal. Today*, 2016, **262**, 170–180.

6 K. Zhu, F. Shi, X. Zhu and W. Wang, *Nano Energy*, 2020, **73**, 104761.

7 E. Willinger, C. Massué, R. Schlgl and M. G. Willinger, *J. Am. Chem. Soc.*, 2017, **139**, 12093–12101.

8 Y. Li, H. Huang, S. Chen, X. Yu, C. Wang and T. Ma, *Nano Res.*, 2019, **12**, 2774–2780.

9 M. Yang, J. Wang, H. Wu and G. W. Ho, *Small*, 2018, **14**, 1703323.

10 Y. Li, M. Cui, C. Wang, Y. Chen, S. Chen, L. Gao, A. Liu, W. Su and T. Ma, *Mater. Today. Energy*, 2020, **17**, 100455.

11 R. K. Kunchala, R. K. Pushpendra and B. S. Naidu, *Sustainable Energy Fuels*, 2022, **6**, 766–777.

12 R. K. Kunchala, R. K. Pushpendra and B. S. Naidu, *ACS Appl. Nano Mater.*, 2021, **4**, 396–405.

13 J. Xie, J. Zhang, S. Li, F. B. Grote, X. Zhang, H. Zhang, R. Wang, Y. Lei, B. Pan and Y. Xie, *J. Am. Chem. Soc.*, 2013, **135**, 17881–17888.

14 M. A. Lukowski, A. S. Daniel, F. Meng, A. Forticaux, L. Li and S. Jin, *J. Am. Chem. Soc.*, 2013, **135**, 10274–10277.

15 G. Zhang, H. Liu, J. Qu and J. Li, *Energy Environ. Sci.*, 2016, **9**, 1190–1209.

16 E. E. Benson, H. Y. Zhang, S. A. Schuman, S. U. Nanayakkara, N. D. Bronstein, S. Ferrere, J. L. Blackburn and E. M. Miller, *J. Am. Chem. Soc.*, 2017, **140**, 441–450.

17 J. Bai, T. Meng, D. Guo, S. Wang, B. Mao and M. Cao, *ACS Appl. Mater. Interfaces*, 2018, **10**, 1678–1689.

18 H. Li, X. Qian, C. Xu, S. Huang, C. Zhu, X. Jiang, L. Shao and L. Hou, *ACS Appl. Mater. Interfaces*, 2017, **9**, 28394–28405.

19 X. Xin, Y. Song, S. Guo, Y. Zhang, B. Wang, Y. Wang and X. Li, *J. Alloys Compd.*, 2020, **829**, 154635.

20 Y. Liu, C. Xiao, M. Lyu, Y. Lin, W. Cai, P. Huang, W. Tong, Y. Zou and Y. Xie, *Angew. Chem.*, 2015, **127**, 11383–11387.

21 H. Wang, Z. Li, G. Li, F. Peng and H. Yu, *Catal. Today*, 2015, **245**, 74–78.

22 S. Dou, L. Tao, J. Huo, S. Wang and L. Dai, *Energy Environ. Sci.*, 2016, **9**, 1320–1326.

23 Y. Yang, H. Yao, Z. Yu, S. M. lslam, H. He, M. Yuan, Y. Yue, K. Xu, W. Hao, G. Sun, H. Li, S. Ma, P. Zapol and M. G. Kanatzidis, *J. Am. Chem. Soc.*, 2019, **141**, 10417–10430.

24 Y. Xi, N. Angulakshmi, B. Zhang, X. Tian, Z. Tang, P. Xie, G. Chen and Y. Zhou, *J. Alloys Compd.*, 2020, **826**, 154201.

25 U. Maitra, B. S. Naidu, A. Govindaraj and C. N. R. Rao, *PNAS*, 2013, **110**, 11704–11707.

26 U. Gupta, B. S. Naidu and C. N. R. Rao, *Dalton Trans.*, 2015, **44**, 472–474.

27 B. S. Naidu, U. Gupta, U. Maitra and C. N. R. Rao, *Chem. Phys. Lett.*, 2014, **591**, 277–281.

28 X. Yu, Y. Feng, Y. Jeon, B. Guan, X. Lou and U. Paik, *Adv. Mater.*, 2016, **28**, 9006–9011.

29 W. Zhang, L. Cui and J. Liu, *J. Alloys Compd.*, 2020, **821**, 153542.

30 J. Dai, D. Zhao, W. Sun, X. Zhu, L. Ma, Z. Wu, C. Yang, Z. Cui, L. Li and S. W. Chen, *ACS Catal.*, 2019, **9**, 10761–10772.

31 L. Diao, B. Zhang, Q. Sun, N. Wang, N. Zhao, C. Shi, E. Liu and C. He, *Nanoscale*, 2019, **11**, 21479–21486.

32 B. Li, Q. Su, L. Yu, J. Zhang, G. Du, D. Wang, D. Han, M. Zhao, S. Ding and B. Xu, *ACS Nano*, 2020, **14**, 17285–17294.

33 M. Wang, K. Jian, Z. P. Lv, D. Li, G. Fan, R. Zhang and J. Dang, *J. Mater. Sci. Technol.*, 2020, **79**, 29–34.

34 J. Wu, X. Wang, J. Jiang, W. Lin, S. Zhu, J. Sha, L. Ma and N. Zhao, *Mater. Lett.*, 2021, **292**, 129621.

35 N. Huang, S. Yan, M. Zhang, Y. Ding, L. Yang, P. Sun and X. Sun, *Electrochim. Acta*, 2019, **327**, 134942.

36 L. He, S. Huang, Y. Liu, M. Wang, B. Cui, S. Wu, J. Liu, Z. Zhang and M. Du, *J. Colloid Interface Sci.*, 2021, **586**, 538–550.

37 X. Zhu, Q. Wu, J. Dai, D. Zhao, C. Yang, L. Li, N. Li and S. Chen, *Electrochim. Acta*, 2021, **384**, 138299.

38 Y. Guo, J. Tang, H. Qian, Z. Wang and Y. Yamauchi, *Chem. Mater.*, 2017, **29**, 5566–5573.

39 F. Du, L. Shi, Y. Zhang, T. Li, J. Wang, G. Wen, A. Alsaedi, T. Hayat, Y. Zhou and Z. Zou, *Appl. Catal., B*, 2019, **253**, 246–252.

40 Y. Guo, J. Tang, Z. Wang, Y. Kang, Y. Bando and Y. Yamauchi, *Nano Energy*, 2018, **47**, 494–502.

41 X. Yang, H. Sun, P. Zan, L. Zhao and J. Lian, *J. Mater. Chem. A*, 2016, **4**, 18857–18867.

42 M. Zheng, J. Du, B. Hou and C. Xu, *ACS Appl. Mater. Interfaces*, 2017, **9**, 26066–26076.

43 M. Bajdich, M. Garcia-Mota, A. Vojvodic, J. K. Norskov and A. T. Bell, *J. Am. Chem. Soc.*, 2013, **135**, 13521–13530.

44 S. Chakrabartty, S. Karmakar and C. R. Raj, *ACS Appl. Nano Mater.*, 2020, **3**, 11326–11334.

45 W. Chen, Y. Liu, Y. Li, J. Sun, Y. Qiu, C. Liu, G. Zhou and Y. Cui, *Nano Lett.*, 2016, **16**, 7588–7596.

46 K. Fan, H. Zou, Y. Lu, H. Chen, F. Li, J. Liu, L. Sun, L. Tong, M. F. Toney, M. Sui and J. Yu, *ACS Nano*, 2018, **12**, 12369–12379.

47 W. Li, D. Xiong, X. Gao and L. Liu, *Chem. Commun.*, 2019, **55**, 8744–8763.

48 G. Huang, Z. Xiao, R. Chen and S. Wang, *ACS Sustainable Chem. Eng.*, 2018, **6**, 15954–15969.

49 L. Yu, B. Xia, X. Wang and X. Lou, *Adv. Mater.*, 2016, **28**, 92–97.